Preparation of $MgIn_2O_4$ Epitaxial Oxide Electrode with Spinel Structure and Heteroepitaxial Growth of $BaTiO_3$-$NiFe_2O_4$ Multiferroic Composite Thin Film

Naoki Wakiya*, Shigeki Sawamura, Kazuki Tanemura, Manami Sano, Naonori Sakamoto, Desheng Fu[1], Kazuo Shinozaki[2], and Hisao Suzuki[1]

Department of Materials Science and Chemical Engineering, Shizuoka University, 3-5-1 Johoku, Naka-ku, Hamamatsu 432-8561, Japan
[1]Graduate School of Science and Technology, Shizuoka University, 3-5-1 Johoku, Naka-ku, Hamamatsu 432-8561, Japan
[2]Department of Metallurgy and Ceramics Science, Tokyo Institute of Technology, 2-12-1 O-okayama, Meguro, Tokyo 152-8550, Japan

An epitaxially grown magnesium indium oxide ($MgIn_2O_4$) thin film was prepared by pulsed laser deposition (PLD) on an yttria-stabilized zirconia (YSZ)-buffered Si substrate at 300°C. Although there is a large lattice mismatch (72.5 %) between $MgIn_2O_4$[100] and YSZ[100], epitaxial growth with cube-on-cube relations, $MgIn_2O_4$(001)//YSZ(001)//Si(001) and $MgIn_2O_4$[100]//YSZ[100]//Si[100], was achieved. A room-temperature electrical conductivity of 290 S/cm and a transmittance >80 % were achieved above 530 nm. The optical band gap measured for a $MgIn_2O_4$ thin film deposited on a glass substrate showed 4.2 eV. On a $MgIn_2O_4$/YSZ/Si(001) substrate, a $BaTiO_3$-$NiFe_2O_4$ composite film was deposited at 700 and 750°C by PLD. Although the partial decomposition of $MgIn_2O_4$ into In_2O_3 was observed, both $BaTiO_3$ and $NiFe_2O_4$ were simultaneously epitaxially grown on $MgIn_2O_4$ with cube-on-cube relation. These findings indicate that $MgIn_2O_4$ can be used as a bottom electrode for multiferroic composite films such as $BaTiO_3$ and $NiFe_2O_4$.

*E-mail address: tnwakiy@ipc.shizuoka.ac.jp

1. Introduction

Recently, a multiferroic concept has been widely accepted. There are two categories of multiferroic materials. One category consists of materials that show ferroelectricity and ferromagnetism (ferrimagnetism) simultaneously in one compound, such as $TbMnO_3$[1], $DyMnO_3$[2], $TbMn_2O_5$[3], $BiFeO_3$[4] or $Ba_{0.5}Sr_{1.5}Zn_2Fe_{12}O_{22}$[5]. The other category consists of composites between ferroelectric and ferromagnetic materials. These composites can be classified into the following four groups, as shown in Fig. 1.: (a) 3-3 type, (b) 2-2 type (bulk), (c) 2-2 type (thin film), and (d) 1-3 type.

The 3-3 type is a three-dimensionally mixed composite of ferroelectric and ferromagnetic bulk materials, and $BaTiO_3$-$Ni(Co,Mn)Fe_2O_4$[6], $Pb(Zr,Ti)O_3$ (PZT)-$Tb_{1-X}Dy_XFe_2$ (Terfenol-D)[7], and $BaTiO_3$-$LaMnO_3$[8] can be classified into this group. The 2-2 type (bulk) is composed of stacked thick sheets of ferroelectric and ferromagnetic materials, and PZT/Terfenol-D/PZT[9-11] and PZT/$NiFe_2O_4$/PZT[12,13] can be classified into this group. The 2-2 type (thin film) is composed of stacked thin films including a superlattice, and PZT/$(La,Sr)MnO_3$[14], $BaTiO_3$/Fe_3O_4[15], and $La_{0.7}Ca_{0.3}MnO_3$/$BaTiO_3$[16] belong to this category. The 1-3 type has a characteristic structure in which ferromagnetic (ferroelectric) nanopillars are embedded in the ferroelectric (ferromagnetic) matrix. Zheng et al. first prepared this type, i.e., a $BaTiO_3$-$CoFe_2O_4$ composite film in which $CoFe_2O_4$ nanopillars are embedded in the $BaTiO_3$ matrix[17]. Since then, many researchers tried to prepare similar thin films between perovskites ($BiFeO_3$, $PbTiO_3$) and spinels ($NiFe_2O_4$, $CoFe_2O_4$)[18-21]. The 1-3 type structure is believed to be formed by self-assembling since perovskites and spinels are immiscible. These 1-3 type composite films have been prepared on $SrTiO_3$(001) single crystals and both perovskites and spinels are epitaxially grown with a (001) orientation. We have prepared a similar $BaTiO_3$-$CoFe_2O_4$ composite epitaxial thin film on a $(La,Sr)CoO_3$ (LSCO)/CeO_2/YSZ-buffered Si(001) substrate[22], which is also epitaxially grown on a perovskite layer (LSCO).

The heteroepitaxial growth of perovskites and spinels is also investigated as a spin-polarized tunnel junctions, such as $La_{2/3}Sr_{1/3}MnO_3$/$SrTiO_3$/$NiFe_2O_4$[23] and Fe_3O_4/$FeGa_2O_4$/$La_{0.7}Sr_{0.3}MnO_3$[24]. In these cases, a $SrTiO_3$ single crystal is also used as a substrate. Thus far, there are only a few reports on the epitaxial growth of a perovskite on a spinel. Ling et al.[25] and Chow et al.[26] prepared epitaxial PZT and $KNbO_3$ thin films, respectively, on $MgAl_2O_4$(001) substrates. However, since $MgAl_2O_4$ is an insulator, it is impossible to measure the electric properties of the perovskite thin film deposited on it. Therefore, it can be considered that epitaxial growth on an electrically conductive spinel satisfies the requirements. The purposes of this work are to prepare a composite film of a perovskite ($BaTiO_3$) and a spinel ($NiFe_2O_4$) on an electrically conductive spinel thin film, and clarify epitaxial relations. As electrically conductive spinels, $MgIn_2O_4$[27], $CdGa_2O_4$[28], and $ZnGa_2O_4$[29] are known. In this work, $MgIn_2O_4$ was selected. $MgIn_2O_4$ thin films have been prepared by several

methods such as pulsed laser deposition (PLD)[30, 31] and chemical spray pyrolysis[32]. All films reported thus far are polycrystalline and there are no reports on the preparation of epitaxially grown films.

2. Experimental Procedure

All films were deposited by pulsed laser deposition (PLD) with a KrF excimer laser (λ = 248 nm) operated at a repetition rate of 7 Hz. The laser beam was focused on each target using a fused silica lens at an angle of 45°. The laser fluence was around 2 J/cm^2. The distance between the target and the substrate was maintained at 55 mm. Both the target and the substrate were rotated during deposition. In this work, the deposition of a $MgIn_2O_4$ thin film was carried out on an $Y_{0.15}Zr_{0.85}O_{1.93}$ (YSZ)-buffered Si(001) substrate, and $BaTiO_3$-$NiFe_2O_4$ (BT-NFO) composite films were deposited on $MgIn_2O_4$. Detailed deposition conditions for preparing YSZ, $MgIn_2O_4$, and $BaTiO_3$-$NiFe_2O_4$ are listed in Table I. Si(001) with natural oxide was cleaned in 2-propanol and used as a substrate. Prior to the deposition of the $MgIn_2O_4$ thin film, the ceramic target with a stoichiometric composition was synthesized by the following procedure: reagent-grade MgO and In_2O_3 powders were mixed and calcined at 800°C for 2 h. Calcined powders were ground and pressed into ceramic disks and sintered at 1300°C for 4 h. The BT-NFO layer was deposited using the sintered ceramic disks composed of 50 mol% $BaTiO_3$ and 50 mol% $NiFe_2O_4$. The thicknesses of YSZ and $MgIn_2O_4$ layers were 20 and 250 nm, respectively. The thickness of the BT-NFO composite film was around 200 nm.

The crystal structure of the thin film was examined using an X-ray diffraction system equipped with a Cu anode (Bruker D8 Advance), and pole figure and reciprocal space map measurements were carried out using a precise X-ray diffractometer (Bruker D8 Discover and Rigaku ATX-G).

The electrical conductivity of the $MgIn_2O_4$ thin film was measured by a 4-probe method and a Keithley 236 source measure unit. The optical transmittance spectrum was measured using a UV-VIS-NIR spectrophotometer (Shimadzu UV-3150). The composition of the film was measured using inductively coupled plasma atomic emission spectroscopy (ICP-AES) (Perkin Elmer Optima 2100DV). Prior to ICP-AES measurement, the film was dissolved in hydrochloric acid.

3. Results and Discussion

3.1. Epitaxial growth of $MgIn_2O_4$ thin film on YSZ/Si(001)

Figure 2 shows the 2θ/ω XRD pattern of the $MgIn_2O_4$/YSZ/Si(001) thin film. This figure indicates that $MgIn_2O_4$ and YSZ films exhibit a c-axis orientation. Figures 3(a)-(c) show (111) X-ray pole figures of Si, YSZ, and $MgIn_2O_4$, respectively. These figures indicate that $MgIn_2O_4$ and YSZ thin films are epitaxially grown on Si(001) substrates with the cube-on-cube relations

$MgIn_2O_4$(001)//YSZ(001)//Si(001) and $MgIn_2O_4$[100]//YSZ[100]//Si[100].

We have reported that a (Ni,Zn)Fe_2O_4 (NZF) thin film deposited on a YSZ-buffered Si(001) substrate exhibits a (111)orientation with NZF(111)//YSZ(001)//Si(001) and NZF[112]//YSZ[100]//Si[100][33]. In the case of NZF/YSZ, the lattice parameters of YSZ and NZF are 0.5139 and 0.8399 nm, respectively. Therefore, if NZF[112]//YSZ[100] is achieved, $(\sqrt{6}/4)a(NZF) = 0.5143\ nm$ (d-spacing along the [112] direction), and the lattice mismatch between this value and the lattice parameter of YSZ is 0.08%. This small lattice mismatch is the reason why (111)epitaxial growth occurs in the case of NZF/YSZ[33]. On the other hand, the lattice parameter of $MgIn_2O_4$ in the ICDD card (#40-1402) is 0.8864 nm; therefore, $(\sqrt{6}/4)a(MgIn_2O_4) = 0.5428\ nm$ and the lattice mismatch between this value and YSZ becomes 5.62%. This large lattice mismatch suggests that $MgIn_2O_4$[112]//YSZ[100] is unfavorable. However, it should be noted that the lattice mismatch between $MgIn_2O_4$ and YSZ is very large (72.5%) in the case of $MgIn_2O_4$[100]//YSZ[100]. This result suggests that lattice mismatch should be considered using multiple numbers of lattices, for example, the lattice mismatch between one lattice of $MgIn_2O_4$ and two lattices of YSZ; the lattice mismatch decreases to -13.8%. In this manner, the lattice mismatch for multiple numbers of lattices can be calculated. Figure 4(a) shows the change in the absolute value of the lattice mismatch between $MgIn_2O_4$[100] and YSZ[100] with the number of spinel lattices. The number of YSZ lattices for obtaining the smallest lattice mismatch is also shown for each number of $MgIn_2O_4$ lattices. This figure indicates that the smallest absolute value of the lattice mismatch is 0.14% between 19 YSZ and 11 $MgIn_2O_4$ lattices. This lattice mismatch value (0.14%) is markedly smaller than that estimated for $MgIn_2O_4$[112]//YSZ[100], as shown by the dotted line in Fig. 4(a). This is the reason why the epitaxial relations of $MgIn_2O_4$(001)//YSZ(001)//Si(001) and $MgIn_2O_4$[100]//YSZ[100]//Si[100] are realized. To ascertain the validity of (111)epitaxial growth for the NZF/YSZ film, a similar consideration was made and is shown in Fig. 4(b). In this case, the smallest absolute value of the lattice mismatch is obtained between 18 YSZ and 11 NZF lattices; however, the value is 0.12%, which is larger than the lattice mismatch for NZF(111)//YSZ(001)//Si(001) and NZF[112]//YSZ[100]//Si[100] (0.08%), as shown by the dotted line in Fig. 4(b).

The electrical conductivity of the $MgIn_2O_4$ thin film measured by a 4-probe method was 290 S/cm. It is known that the electrical conductivity of the $MgIn_2O_4$ thin film markedly changes with

deposition conditions. The $MgIn_2O_4$ thin film deposited by RF sputtering followed by postannealing at 300°C in H_2 shows 230 S/cm[34]. Kudo et al. reported that electrical conductivity changed with oxygen pressure during deposition between 0.5 and 1300 S/cm, and the maximum conductivity was obtained at an oxygen pressure of 1.0×10^{-5} Torr[30]. In our work, the film was deposited at an oxygen pressure of 5.5×10^{-4} Torr; therefore, the value of conductivity agrees well with those previously reported. The optical transmittance spectrum of the $MgIn_2O_4$ thin film deposited on silica glass is shown in Fig. 5. This figure depicts that 90.5% of transmittance is achieved above the 530 nm wavelength. This indicates that this film is a transparent electrode. The optical band gap of the $MgIn_2O_4$ film was evaluated by analyzing an $(\alpha h\nu)^2$ vs $h\nu$ plot (inset of Fig. 5), where α is the absorption coefficient, h is Plank's constant, and ν is the frequency.

The absorption coefficient α is calculated as

$$\alpha = -\frac{\ln(1/T)}{t},$$

where T is the optical transmittance, and t is the thickness. As shown in the inset of Fig. 5, the optical band gap was estimated to be 4.2 eV. This value is larger than the reported value of 3.4 eV[27]. Raj et al. examined the effect of Mg/In ratio on optical band gap for the $MgIn_2O_4$ thin film prepared by chemical spray pyrolysis[32]. They reported that optical band gap varied from 3.18 to 3.86 eV ($0.35<Mg/In<0.5$). Their results suggest that optical band gap increases with Mg content. We tried to measure the film composition using ICP-AES. Therefore, as the film composition, Mg/In=0.6 was obtained. The large optical band gap of 4.2 eV obtained in this work is due to the Mg-rich composition.

3.2. Crystal structure of $BaTiO_3$-$NiFe_2O_4$ composite film

Figure 6 shows XRD patterns of the $BaTiO_3$-$NiFe_2O_4$ composite thin film deposited on $MgIn_2O_4$/YSZ/Si(001) at (a) 700°C (in 10 mTorr O_2) and (b) 750°C (in 100 mTorr O_2). Figures 6 (a) and (b) indicate the peaks of polycrystalline In_2O_3 and the peak of $MgIn_2O_4$(004). The formation of In_2O_3 suggests that $MgIn_2O_4$ is partially decomposed. According to the phase diagram, $MgIn_2O_4$ is a stable phase at least up to 1350°C[35]. Therefore, we consider that the reason why $MgIn_2O_4$ was partially decomposed above 700°C is that the film was deposited at 300°C since Kudo et al. reported that a $MgIn_2O_4$ thin film with a high electrical conductivity is prepared at 300°C[30]. To improve thermal stability, the deposition conditions of $MgIn_2O_4$ should be improved. The inset of Fig. 6 shows a zoomed area between 42 and 46° in 2θ. A single peak is observed at around 44.2° in 2θ for the film deposited at 700°C in 10 mTorr O_2. The diffraction peak lies between those of $NiFe_2O_4$(004) and $BaTiO_3$(002). On the other hand, peak broadening with a shoulder on the large-angle side is observed in the film deposited at 750°C in 100 mTorr O_2. The position of the broadened shoulder corresponds to $BaTiO_3$(002). Note that no peak broadening is observed in the film deposited at

700°C in 100 mTorr O_2 nor at 750°C in 10 mTorr O_2. A similar phenomenon has been reported by Zheng et al.[36]. They prepared a $BaTiO_3$-$CoFe_2O_4$ composite film and reported that the film deposited at 700°C was "supersaturated" and no peak splitting was observed. They also found that peak splitting occurs above 800°C.

In this work, the orientation relation of the $BaTiO_3$-$NiFe_2O_4$ thin film deposited on $MgIn_2O_4$/YSZ/Si(001) was also examined. Figure 7 shows the X-ray pole figures of (a)Si(111), (b)$BaTiO_3$(111), and (c)$NiFe_2O_4$(111) measured for the $BaTiO_3$-$NiFe_2O_4$ film deposited at 700°C. This figure depicts that both $BaTiO_3$ and $NiFe_2O_4$ are epitaxially grown with cube-on-cube relations on Si via YSZ and $MgIn_2O_4$. This indicates that an epitaxial relation was maintained, though the partial decomposition of $MgIn_2O_4$ was observed as mentioned above. The mechanism between the partial decomposition and the continuance of epitaxial growth is considered as the low decomposition rate of $MgIn_2O_4$, such that epitaxial growth was achieved before partial decomposition. This mechanism is confirmed by cross-sectional TEM observation. This work is in progress now.

4. Conclusions

We deposited $MgIn_2O_4$ thin films on YSZ/Si(001) and glass substrates by pulsed laser deposition at 300°C. On the YSZ/Si(001) substrate, cube-on-cube epitaxial growth [$MgIn_2O_4$(001)//YSZ(001)//Si(001) and $MgIn_2O_4$[100]//YSZ[100]//Si[100]] was achieved, though the lattice mismatch between $MgIn_2O_4$ and YSZ was very large (72.5%). This epitaxial relation is different from that observed for NZF/YSZ [NZF(111)//YSZ(001)//Si(001) and NZF[112]//YSZ[100]//Si[100]]. The difference in epitaxial relation was explained by considering the lattice mismatch using multiple numbers of lattices. A room-temperature electrical conductivity of 290 S/cm was obtained. A transmittance >80 % was achieved above 530 nm and an optical band gap of 4.2 eV was observed for $MgIn_2O_4$ deposited on the glass substrate. On the epitaxial $MgIn_2O_4$/YSZ/Si(001) substrate, a $BaTiO_3$-$NiFe_2O_4$ composite film was deposited at 700 and 750°C by PLD. Although the partial decomposition of $MgIn_2O_4$ into In_2O_3 was observed, both $BaTiO_3$ and $NiFe_2O_4$ were simultaneously epitaxially grown on $MgIn_2O_4$ with cube-on-cube relations. These findings indicate that $MgIn_2O_4$ can be used as a bottom electrode for multiferroic composite films, such as $BaTiO_3$ and $NiFe_2O_4$.

Acknowledgements

The authors thank Dr. K. Saito and H. Morioka of Bruker AXS for assistance with X-ray diffraction measurement. This work was supported by a Grant-in-Aid for Scientific Research (No. 19360296) from the Ministry of Education, Culture, Sports, Science and Technology, and Asahi Glass Foundation.

References

1) T. Kimura, T. Goto, H. Shintani, K. Ishizaka, T. Arima, and Y. Tokura: Nature **426** (2003) 55.

2) T. Kimura, G. Lawes, T. Goto, Y. Tokura, and A. P. Ramirez: Phys. Rev. B **71** (2005) 224425.

3) N. Hur, S. Park, P. A. Sharma, J. S. Ahn, S. Guha, and S. W. Cheong: Nature **429** (2004) 392.

4) J. Wang, J. B. Neaton, H.Zheng, V. Nagarajan, S. B. Ogale, B. Liu, D. Viehland, V. Vaithyanathan, D. G.. Schlöm, U. V. Waghmare, N. A. Spaldin, K. M. Rabe, M. Wuttig, and R. Ramesh: Science **299** (2002) 1719.

5) N. Momozawa, and Y. Yamaguchi: J. Phys. Soc. Jpn. **62** (1993) 1292.

6) J. van den Boomgaard, and R. A. J. Born: J. Mater. Sci. **13** (1978) 1538.

7) C. W. Nan, N. Cai, L. Liu, J. Zhai, Y. Ye, and Y. Lin: J. Appl. Phys. **94** (2003) 5930.

8) K. Ban, M. Gomi, T. Shundo, and N. Nishimura: IEEE Trans. Magn. **41** (2005) 2793.

9) G. Liu, C. W. Nan, N. Cai, and Y. Lin: J. Appl. Phys. **95** (2004) 2660.

10) G. Liu, C. W. Nan, N. Cai, and Y. Lin: J. Solid Struct. **41** (2004) 4423.

11) N. Cai, C. W. Nan, J. Zhai, and Y. Lin: Appl. Phys. Lett. **84** (2004) 3516.

12) J. Zhai, N. Cai, Z. Shi, Y. Lin, and C. W. Nan: J. Appl. Phys. **95** (2004) 5685.

13) G. Srinivasan, E. T. Rasmussen, A. A. Bush, K. E. Kamentsev, V. F. Meshcheryakov, and Y. K. Fetisov: Appl. Phys. A **78** (2004) 721.

14) H. Tabata and T. Kawai: IEICE Trans. Electron. **E-80C** (1997) 918.

15) M. Ziese, A. Bollero, I. Panagiotopoulos, and N. Moutis: Appl. Phys. Lett. **88** (2006) 212502.

16) M. P. Singh, W. Prellier, L. Mechin, C. Simon, and B. Raveau: J. Appl. Phys. **99** (2006) 024105.

17) H. Zheng, J. Wang, S. E. Lofland, Z. Ma, L. M. Ardabili, T. Zhao, L. S. Riba, S. R. Shinde, S. B. Ogale, F. Bai, D. Viehland, Y. Jia, D. G. Schlöm, M. Wuttig, A. Roytburd, and R. Ramesh: Science **303** (2004) 661.

18) W. Chen, Z. H. Wang, C. Ke, W. Zhu, O. K. Tan: Mater. Sci. Eng. B **162** (2009) 47.

19) I. Levin, J. Li, J. Slutsker, and A. L. Roytburd: Adv. Mater. **18** (2006) 2044.

20) Q. Zhan, R. Yu, S.P. Crane, H. Zheng, C. Kisielowski, and R. Ramesh: Appl. Phys. Lett. **89** (2006) 172902.

21) R. Muralidharan, N. Dix, V. Skumryev, M. Varela, F. Sánchez, and J. Fontcuberta: J. Appl. Phys. **103** (2008) 07E301.

22) S. Sawamura, N. Wakiya, N. Sakamoto, K. Shinozaki and H. Suzuki: Jpn. J. Appl. Phys. **47** (2008) 7603.

23) U. Lüders, G. Herranz, M. Bibes, K. Bouzehouane, E. Jacquet, J.P Contour, S. Fusil, J.F. Bobo, J. Fontcuberta, A. Barthélémy, and A. Fert: J. Appl. Phys. **99** (2006) 08K301.

24) L. M. B. Alldredge, R. V. Chopdekar, B. B. Nelson-Cheeseman, and Y. Suzuki: Appl. Phys. Lett. **89** (2006) 182504.

25) S. H. Ling, Y. S. Tang, W. S. Au, and H. K. Wong: Appl. Phys. Lett. **62** (1993) 1757.

26) A. F. Chow, D. J. Lichtenwalner, R. R. Woolcott, Jr., T. M. Graettinger, O. Auciello, A. Kingon, L. A. Boatner, and N. R. Parikh: Appl. Phys. Lett. **65** (1994) 1073.

27) N. Ueda, T. Omata, N. Hikuma, K. Ueda, H. Mizoguchi, T. Hashimoto, and H. Kawazoe: Appl. Phys. Lett. **61** (1992) 1954.

28) T. Omata, N. Ueda, N. Hikuma, K. Ueda, H. Mizoguchi, T. Hashimoto, and H. Kawazoe: Appl. Phys. Lett. **62** (1993) 499.

29) T. Omata, N. Ueda, K. Ueda, and H. Kawazoe: Appl. Phys. Lett. **64** (1994) 1077.

30) A. Kudo, H. Yanagi, H. Hosono, and H. Kawazoe: Mater. Sci. Eng. B **54** (1998) 51.

31) M. Miyakawa, K. Ueda, and H. Hosono: Nucl. Instrum. Methods Phys. Res. Sect. B **191** (2002) 173.

32) A. M. E. Raj, V. Senthilkumar, V. Swaminathan, J. Wollschläger, M. Suendorf, M. Neumann, M. Jayachandran, and C. Sanjeeviraja: Thin Solid Films **517** (2008) 510.

33) N. Wakiya, K. Shinozaki, and N. Mizutani: Jpn. J. Appl. Phys. **41** (2002) 7242.

34) H. Un'no, N. Hikimura, T. Omata, N. Ueda, T. Hashimoto, and H. Kawazoe: Jpn. J. Appl. Phys. **32** (1993) 1260.

35) N. Kimizuka, T. Mohri, and M. Nakamura: J. Solid State Chem. **81** (1989) 70.

36) H. Zheng, J. Kreisel, Y. H. Chu, R. Ramesh, and L. Salamanca-Riba: Appl. Phys. Lett. **90** (2007) 113113.

List of captions

Table I. Deposition conditions of $BaTiO_3$-$NiFe_2O_4$/$MgIn_2O_4$/YSZ thin film on Si(001) substrate.

Fig. 1. Schematic illustration of composite in (a) the 3-3 type where both ferroelectric and ferromagnetic bulk are 3-dimensionally mixed, and in (b) the 2-2 type (bulk) where thick sheets of ferroelectric and ferromagnetic materials are stacked, and in (c) the 2-2 type (thin film) where thin films of ferroelectric and ferromagnetic materials are deposited on substrates, and in (d) the 1-3 type where ferromagnetic (ferroelectric) nanopillars are embedded in the ferroelectric (ferromagnetic) matrix.

Fig. 2. X-ray diffraction pattern of $MgIn_2O_4$/YSZ/Si(001) thin film.

Fig. 3. X-ray pole figures of $MgIn_2O_4$/YSZ/Si(001) thin film.
(a) Si(111), (b) YSZ(111), and (c) $MgIn_2O_4$(111).

Fig. 4. Change in absolute value of lattice mismatch between spinel[100] and YSZ[100] with number of spinel lattices. The number of YSZ lattices for the smallest lattice mismatch is also shown.
(a) Lattice mismatch between $MgIn_2O_4$ and YSZ, and (b) that between NZF and YSZ.
The dotted line shows the lattice mismatch between spinel[112] and YSZ[100].

Fig. 5. Optical transmittance spectrum of the $MgIn_2O_4$ films deposited on glass.
The inset shows the optical band gap estimation.

Fig. 6. X-ray diffraction pattern of $BaTiO_3$-$NiFe_2O_4$ film deposited on
$MgIn_2O_4$/YSZ/Si(001) deposited at (a) 700 and (b) 750^{o}C.

Fig. 7. X-ray pole figures of $BaTiO_3$-$NiFe_2O_4$ thin film deposited on $MgIn_2O_4$/YSZ/Si(001).
(a) Si(111), (b) $BaTiO_3$(111), and (c) $NiFe_2O_4$(111).

Table I. Deposition conditions of $BaTiO_3$-$NiFe_2O_4$/$MgIn_2O_4$/YSZ thin film on Si(001) substrate.

	Deposition temperature (^oC)	Deposition pressure (Torr)	Thickness (nm)
YSZ	800	$5.5x10^{-4}$	20
$MgIn_2O_4$	300	$5.5x10^{-4}$	250
$BaTiO_3$-$NiFe_2O_4$	700, 750	$1.0x10^{-2}$, $1.0x10^{-1}$	200

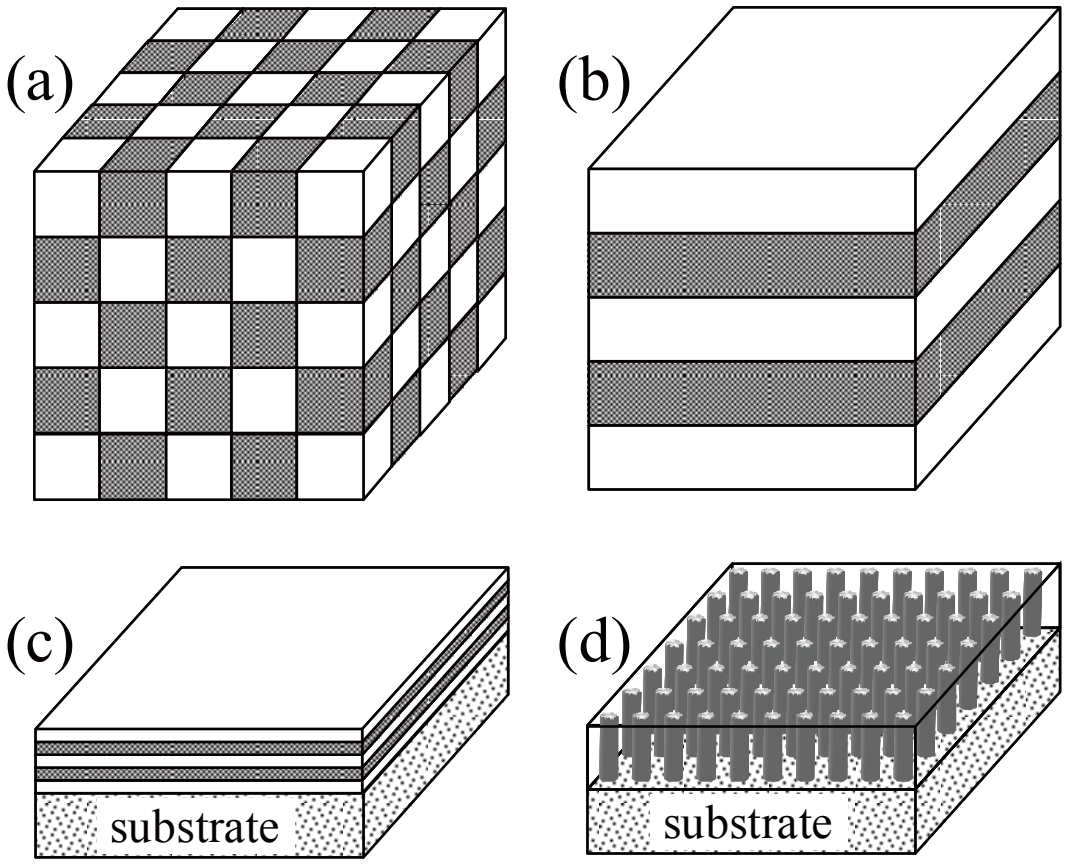
(a)
(b)
(c)
substrate
(d)
substrate

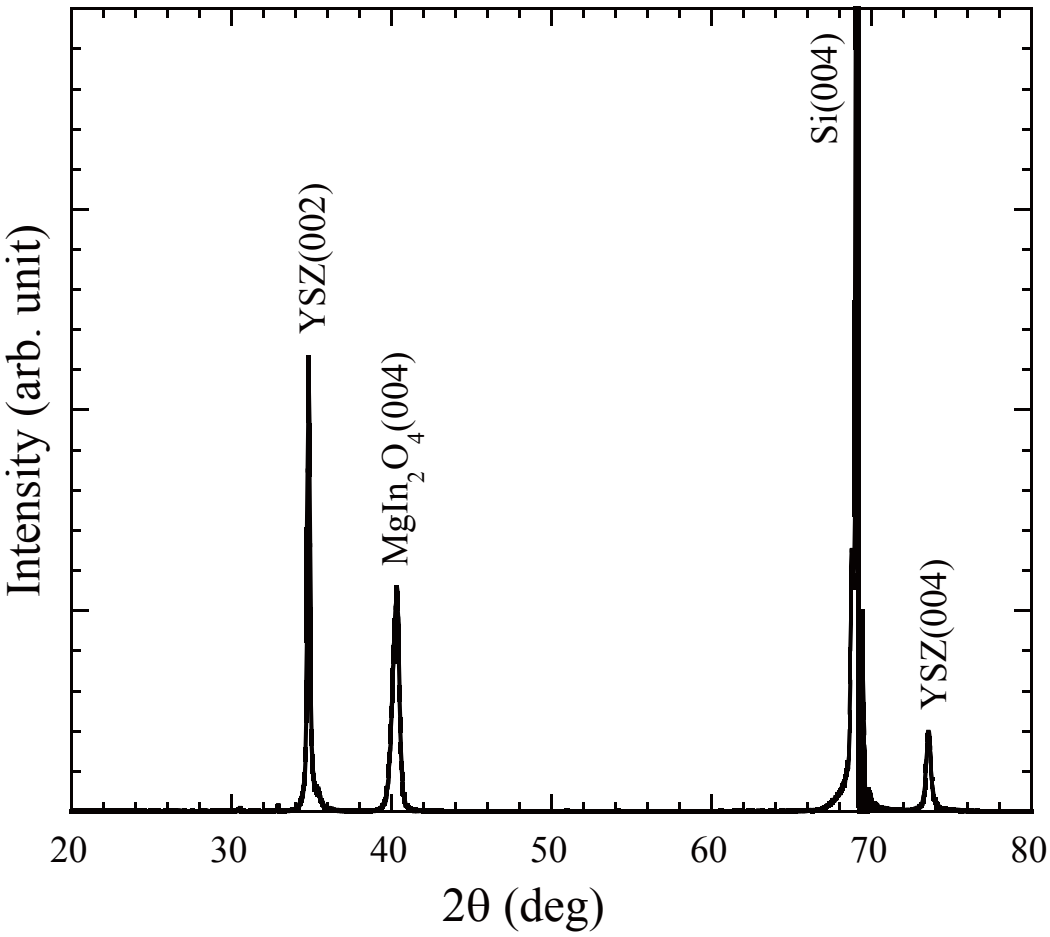
Intensity (arb. unit)
YSZ(002)
MgIn2O4(004)
Si(004)
YSZ(004)
20
30
40
50
60
70
80
2θ (deg)

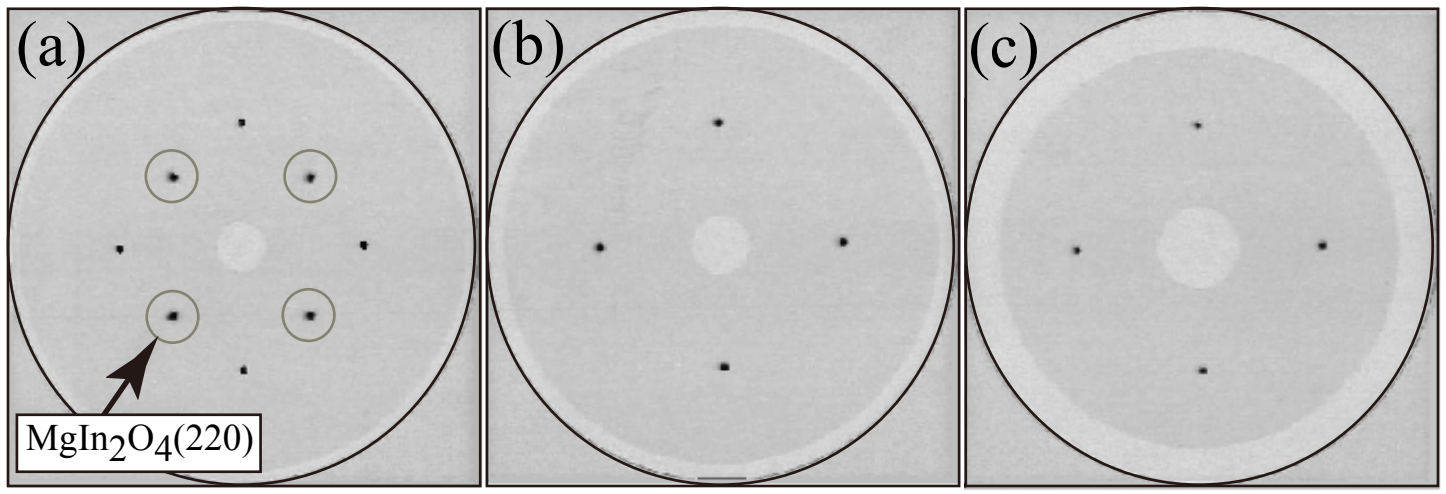
(a)
(b)
(c)
MgIn2O4(220)

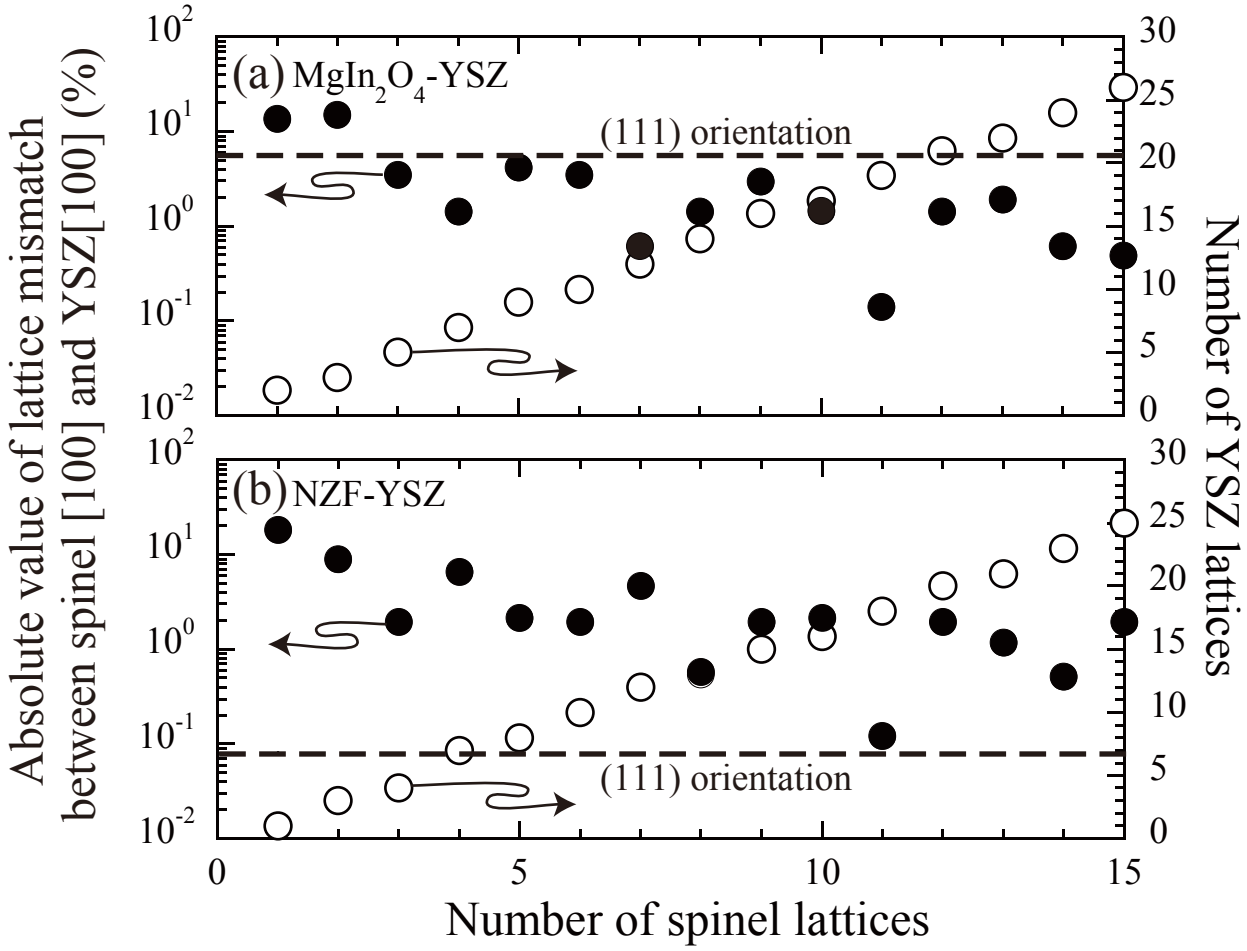
(a) MgIn2O4-YSZ
(111) orientation
(b) NZF-YSZ
(111) orientation
Absolute value of lattice mismatch between spinel [100] and YSZ[100] (%)
Number of YSZ lattices
Number of spinel lattices
10^2
10^1
10^0
10^-1
10^-2
30
25
20
15
10
5
0
0
5
10
15

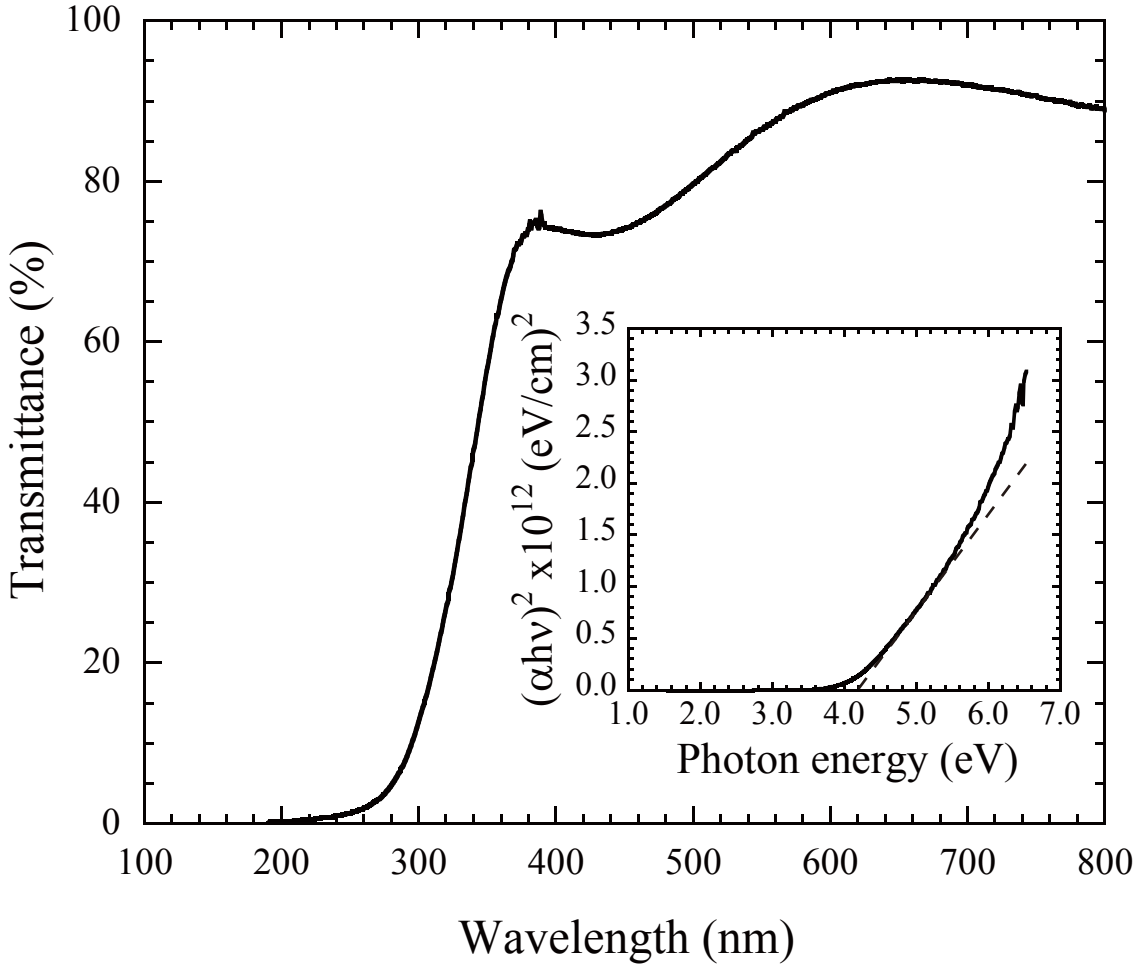
Transmittance (%)
Wavelength (nm)
100
80
60
40
20
0
100
200
300
400
500
600
700
800
$(\alpha h\nu)^2$ x10^{12} (eV/cm)^2
Photon energy (eV)
3.5
3.0
2.5
2.0
1.5
1.0
0.5
0.0
1.0
2.0
3.0
4.0
5.0
6.0
7.0

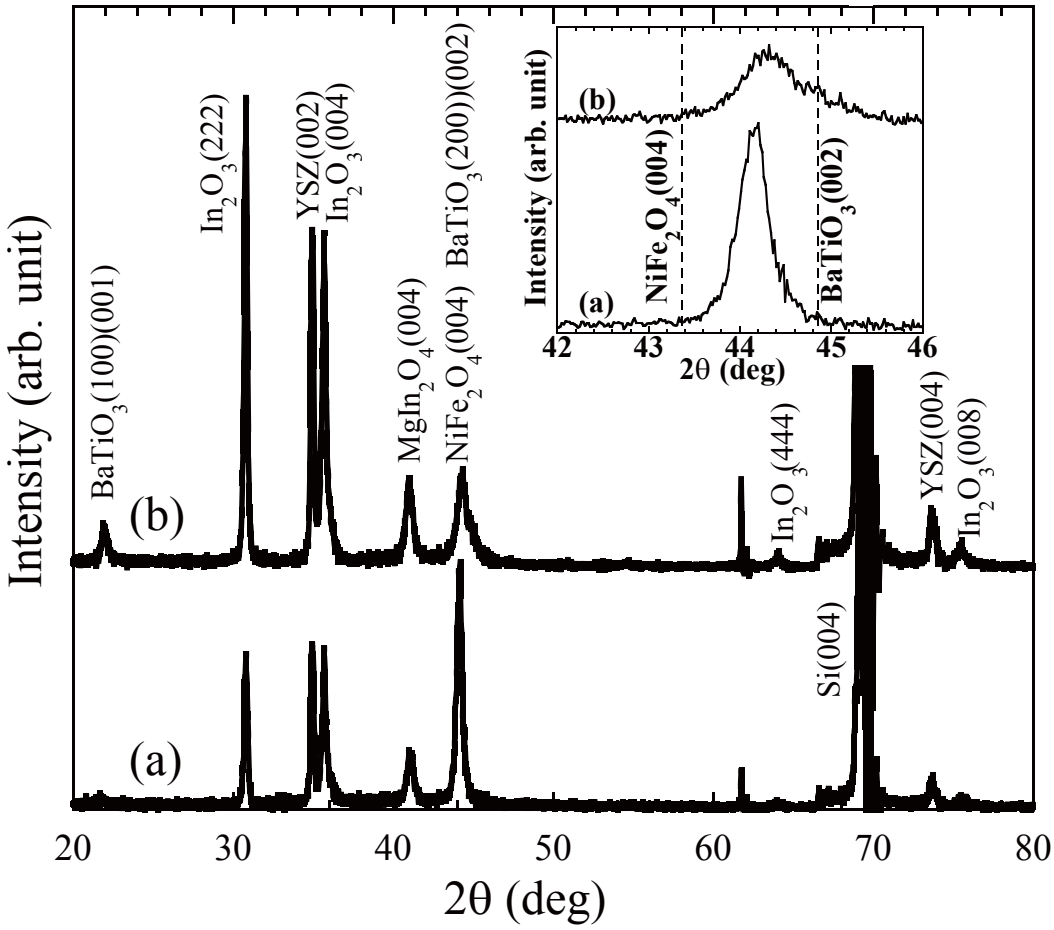
Intensity (arb. unit)
2θ (deg)
20
30
40
50
60
70
80
BaTiO3(100)(001)
In2O3(222)
YSZ(002)
In2O3(004)
MgIn2O4(004)
NiFe2O4(004)
BaTiO3(200))(002)
In2O3(444)
YSZ(004)
In2O3(008)
Si(004)
(a)
(b)
Intensity (arb. unit)
NiFe2O4(004)
BaTiO3(002)
42
43
44
45
46
2θ (deg)

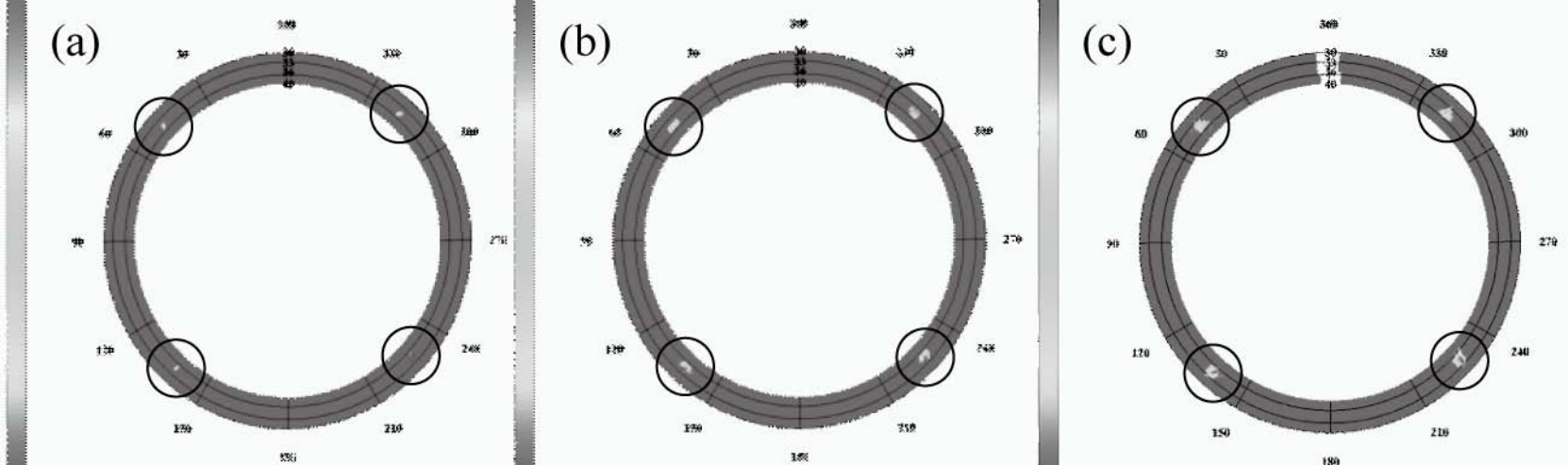
(a)
(b)
(c)